I.   ESTIMATION OF UNCERTAINTY

The conclusions regarding the dimensionality of the different superconducting phases (main text Fig. 3) depend strongly on the degree of uncertainty in the determination of H_1 and H_2, so it is important to estimate how accurate this is. The method used to determine these fields is outlined in Fig. S2(b). In the case of H_1, an estimate of the uncertainty can be made from the width of the dip in the second derivative. A sharper dip corresponds to a smaller error.

In the case of H_2, the uncertainty depends on the determination of R_N. In magnetic fields just above the characteristic field, the resistivity is fairly flat, but there is, nevertheless, a finite magnetoresistance that can introduce a potential error here. In parallel field, the resistance upturn above H_2 increases the error.

The error bars in Fig. 4 (c)-(e) are extracted from the width of the region in the differential resistivity curves where the resistivity drops strongly. At higher temperatures or fields, this region becomes more smeared out and less well defined, leading to larger error bars.

II.   FITTING

The actual models used to do the fitting in Fig. 3 of the main text are as follows. The 3D Ginzburg-Landau model:

$$\left(\frac{H_c \sin \theta}{H_{c\parallel}}\right)^2 + \left(\frac{H_c \cos \theta}{H_{c\perp}}\right)^2 = 1$$

The 2D Tinkham model:

$$\left(\frac{H_c \sin \theta}{H_{c\parallel}}\right)^2 + \left|\frac{H_c \cos \theta}{H_{c\perp}}\right| = 1$$

Additionally, for Fig. S3, the Yamafuji thin film model:

$$\frac{H_c \sin \theta}{H_{c\parallel}} + \left(\frac{H_c \cos \theta}{H_{c\perp}}\right)^2 \left[1 - 3(1+\sqrt{2})\left(\frac{H_{c\parallel}}{H_{c\perp}}\right)^2 \frac{H_c \sin \theta}{H_{c\parallel}}\right] = 1$$

The Yamafuji surface layer model:

$$\frac{H_c \sin \theta}{H_{c\parallel}} + \left(\frac{H_c \cos \theta}{H_{c\perp}}\right)^2 [1 + \tan \theta(1 - \sin \theta)] = 1$$

III.   SAMPLE DIMENSIONS

TABLE S1. Dimensions of the different FIB-fabricated samples used in this study. Note that two different sets of dimensions are quoted for sample 2, as this sample was measured, modified and then measured again. Its behaviour was unchanged after this modification.

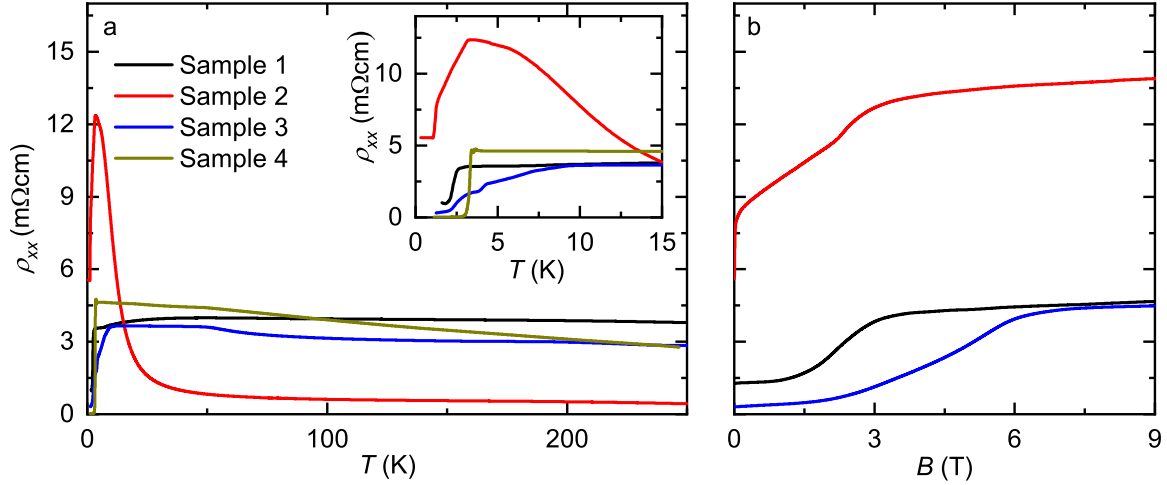| Sample	Width (μm)	Thickness (μm)	Length (μm)
1	26.5	13.9	34
2a	13	4.2	22
2b	4.2	4.2	22
3	6.6	6.7	32
4	9.5	7.0	16

IV. SUPPLEMENTARY FIGURES

FIG. S1. **a** Temperature sweeps of the resistivity of each of the four measured TaP crystals made with FIB. Inset: the same data, but focused on the low temperature part in order to show the superconducting transitions. The reason for the more semiconducting behavior of sample 2 is not understood. Sample 3 is oriented with the current along the c-axis while the other samples are mounted with the current aligned with the ab-plane. Apart from sample 2, all microsamples have an RRR$\approx$1. The non-metallic behavior seen in our FIB-processed samples may be caused by the FIB-prepared electrical contacts. The deposition of platinum by FIB is not an ideal method of preparing clean contacts and may lead to spurious resistances. The surface damage to the sample caused by FIB can (at least above T_c) worsen this effect. **b** Field sweeps made with magnetic field perpendicular to the current direction of the samples 1, 2 and 3, demonstrating a partial superconducting transition.
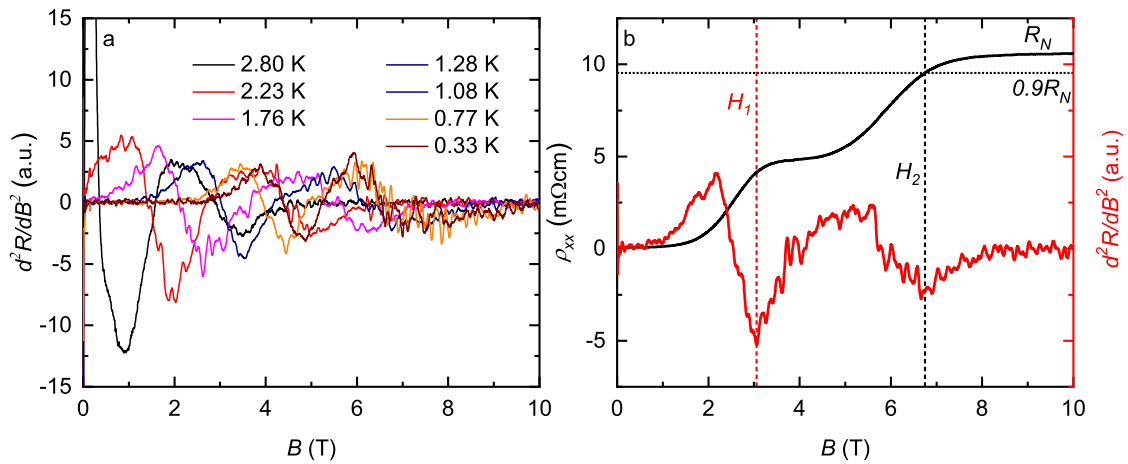

FIG. S2. **a** Representative second derivatives of the temperature-dependent field sweeps for sample 4, used to identify the transition field H_1. **b** Illustration of how the identification of the characteristic fields was achieved: H_2 is the field where the resistivity reaches 90% of the normal state value and H_1 is identified by the first negative peak in the second derivative.
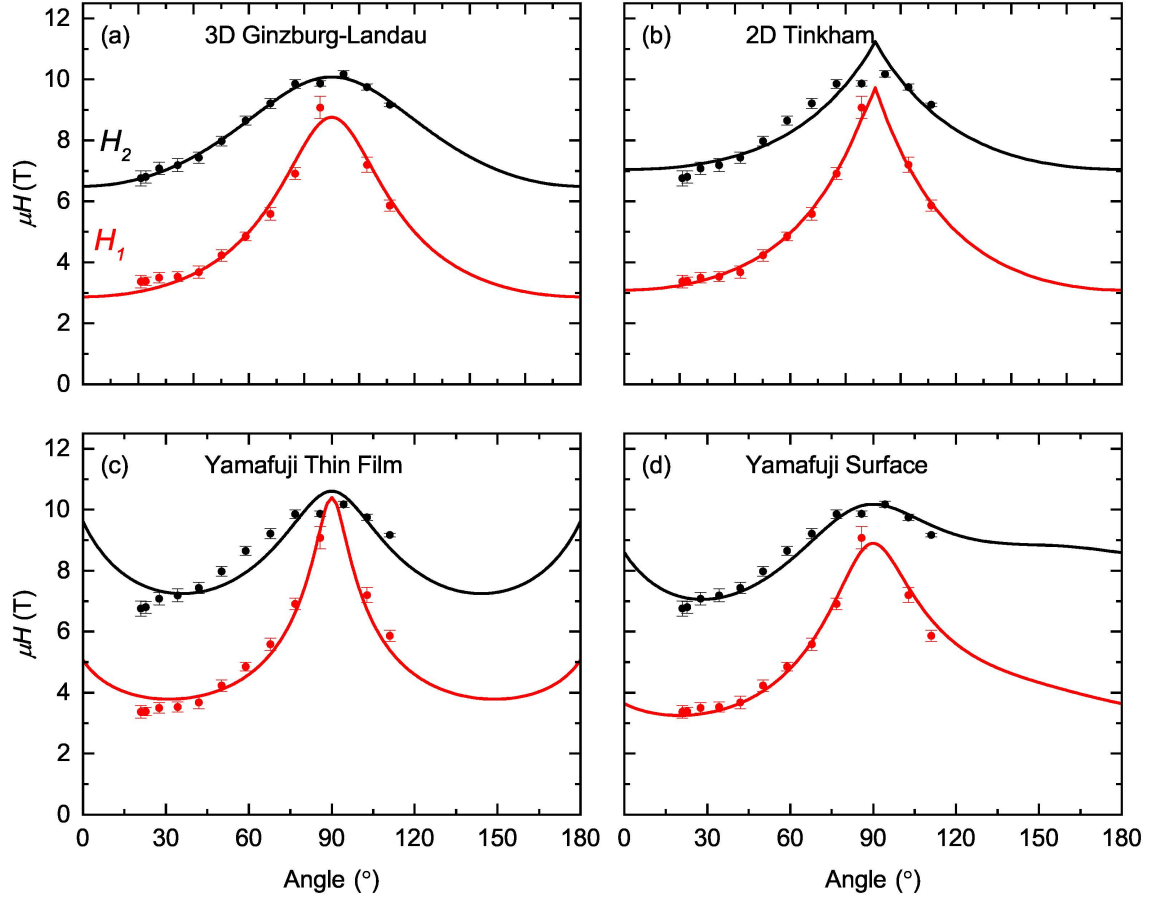
FIG. S3. Angle dependence of characteristic fields (extended version of main Figure 3), fitted with (**a**) the 3D Ginzburg-Landau model, (**b**) the 2D Tinkham model, (**c**) the Yamafuji model for thin films and (**d**) the Yamafuji model for surface superconductivity.
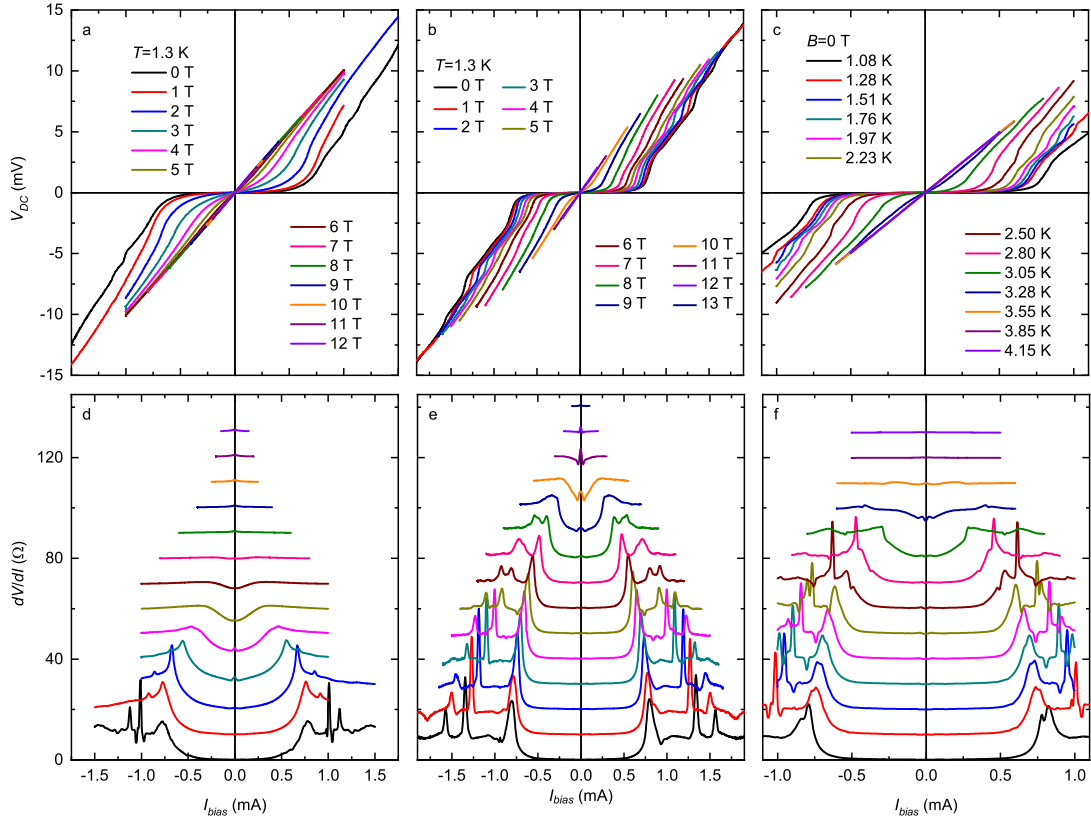
FIG. S4. IV curves and differential resistance dV/dI of sample 4 measured **a** and **d** for fields up to 12 T perpendicular to the current direction; **b** and **e** for parallel fields and **c** and **f** for different temperatures between 1 and 4.15 K.
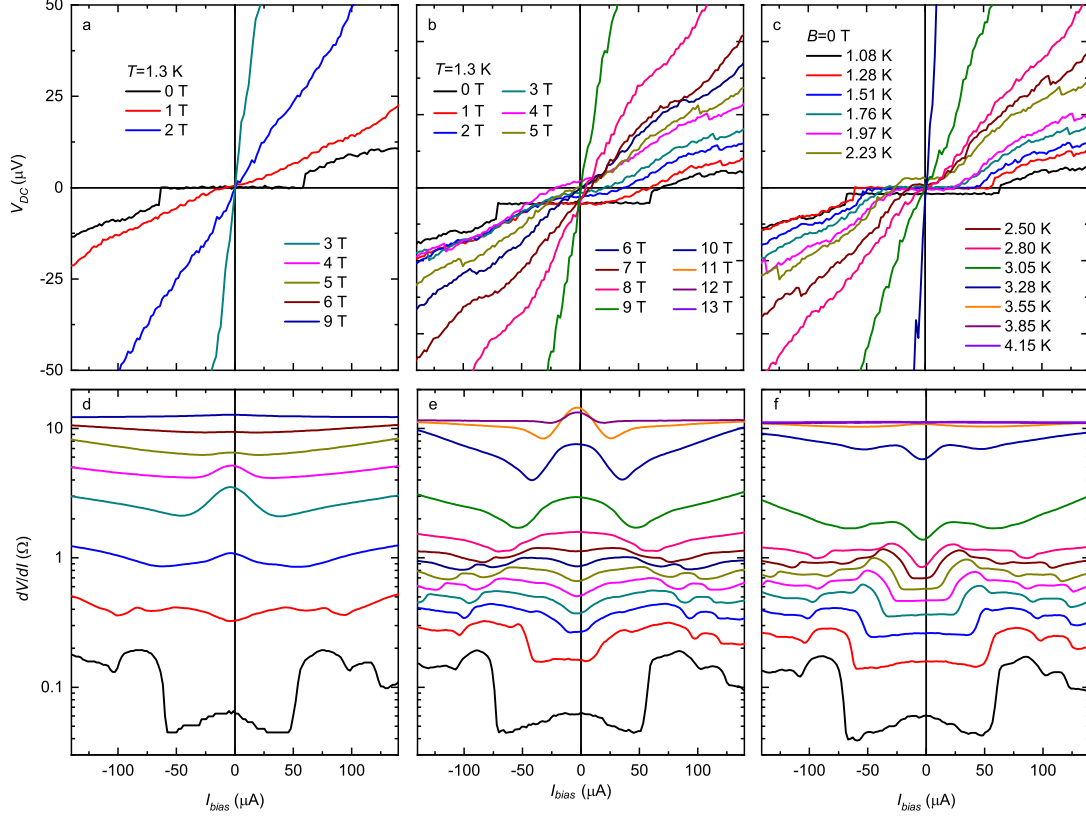
FIG. S5. Same data as Fig. S4, focused on the small current region to highlight the critical current due to the surface mechanism. **a** and **d** IV and dV/dI for perpendicular fields; **b** and **e** for parallel fields and **c** and **f** for different temperatures.
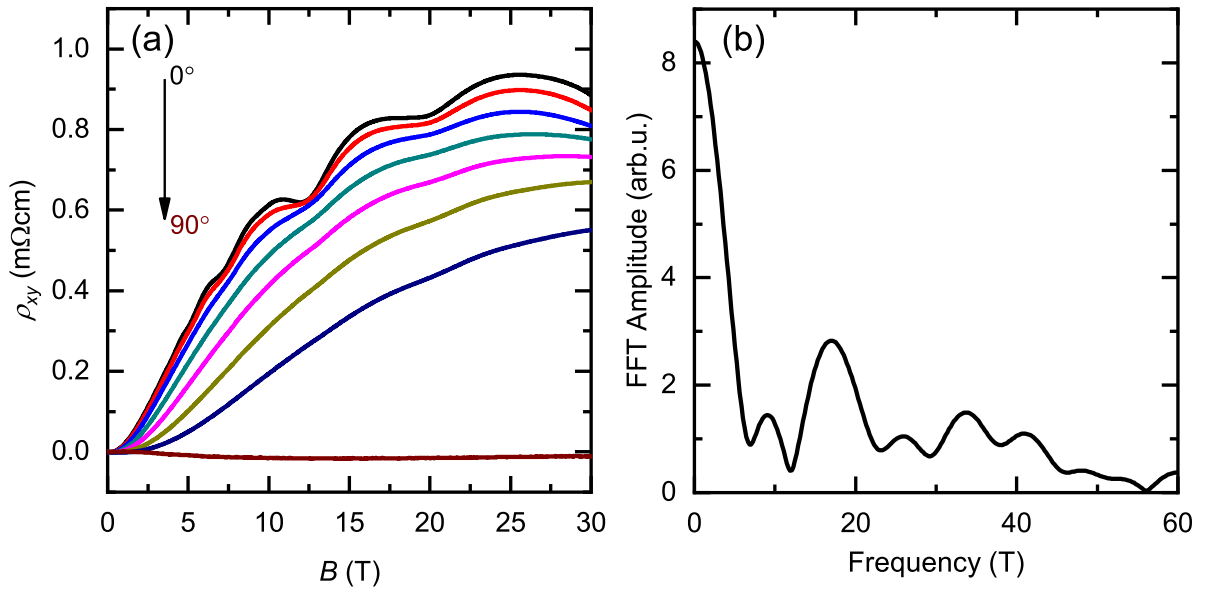

FIG. S6. Demonstration of quantum oscillations in the FIB-processed TaP, showing that at least a part of the crystal is of high quality. **a** Hall resistivity of sample 4 at $T = 4.2$ K for different angles between the magnetic field and the c-axis of the sample, showing clear oscillations and **b** the Fast Fourier transform (FFT) of the $B \parallel c$ data in **a**.
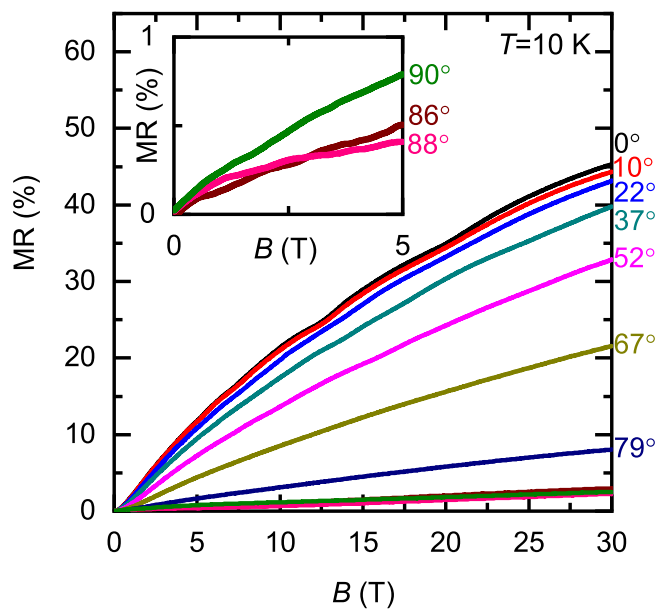
FIG. S7. Magnetoresistance data for sample 1, under different angles. Inset: highlight of the low-field data close to $B \parallel I$, showing the absence of negative magnetoresistance.
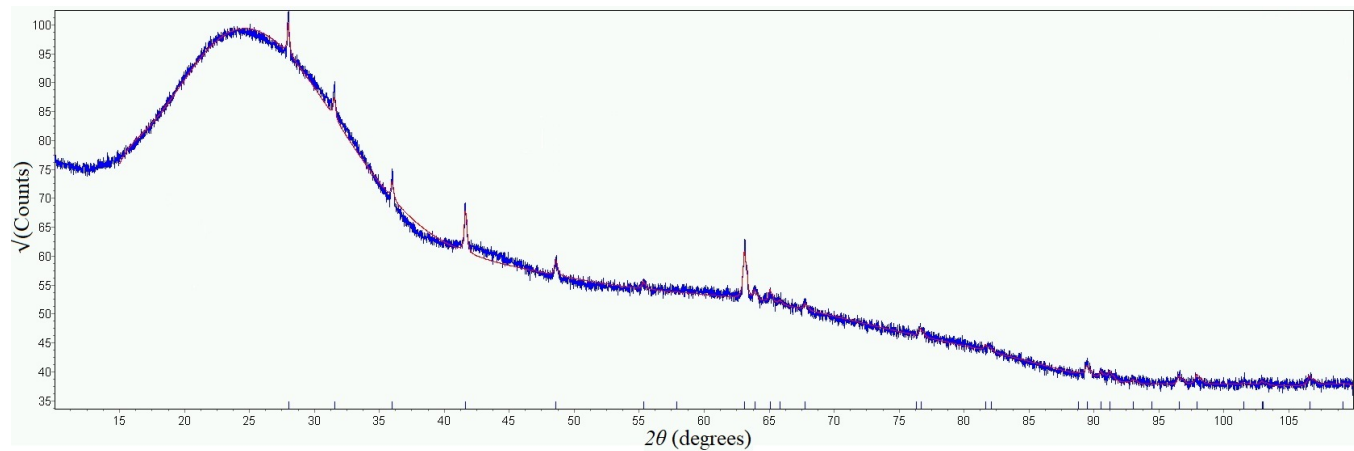

FIG. S8. Powder XRD spectrum of our TaP crystal. Blue ticks on the x-axis indicate where diffraction peaks from the tetragonal structure are expected. The blue curve is the experimental data and the red curve the modeled diffraction pattern of the tetragonal TaP structure (including a background curve).